Journal of Solid State Electrochemistry
https://doi.org/10.1007/s10008-023-05592-w

ORIGINAL PAPER

Electrochemical characterization of Al–Li alloys AA2099 and AA2055 for aeronautical applications: effect of thermomechanical treatments

H. Rivera Cerezo[1] · C. Gaona Tiburcio[1] · J. A. Cabral Miramontes[1] · Raúl Germán Bautista-Margulis[2] · D. Nieves Mendoza[3] · E. Maldonado Bandala[3] · F. H. Estupiñán-López[1] · F. Almeraya Calderón[1]

Received: 30 December 2022 / Revised: 2 July 2023 / Accepted: 6 July 2023

Abstract

Third-generation Al–Li alloys are high-performance materials that are very attractive for aircraft and aerospace applications due to their relatively low density, high specific strength, and stiffness. To study the effect of heat treatments on the electrochemical behavior of two high-performance aluminum-lithium alloys, in this work the electrochemical noise technique was used to evaluate the corrosion behavior of AA2099 and AA2055 alloys under three conditions of different heat treatments, an annealing treatment (T0), a second treatment in solid solution, followed by rapid cooling (quenching) and subsequent artificial aging (T6), and a third treatment in solid solution, tempering, cold deformation, and maturation artificial (T8). The time series obtained from the electrochemical noise tests were visually analyzed, as well as the statistical parameters such as localization index (LI), bias, and kurtosis. Analysis in the frequency domain was also performed by means of power spectral density (PSD) signals. In general, it was observed that the distribution of precipitates on the surface of the alloys considerably affects the corrosion performance, as well as the concentration of Cl-1 ions in the test electrolytes.

Keywords Aluminum-lithium alloy · T1 phase · Electrochemical noise · Precipitation · Corrosion

Introduction

Third-generation aluminum-lithium alloys have generated interest in the aviation and aerospace industry due to their excellent mechanical properties, low density, and corrosion resistance [1–4]. It is known that in Al–Li alloys, for every 1% by weight of Li added, the density of the alloy is reduced by 3%, while the Young's modulus increased by 6% [5]. In this series of Al–Li alloys, the Cu/Li ratio is increased compared to previous generations. Other minor alloying elements such as Ag and Zn are added, and the Li content is less than 2% by weight. This is the main characteristic that gives the alloy better properties than its predecessor generations [6–8].

These alloys have great potential to replace the traditionally used aluminum alloys of the 2xxx and 7xxx series. They find application in different aircraft structures, such as fuselage skins, wings, doors, windows, etc. [9, 10]. Currently, research has been carried out on the electrochemical behavior of Al–Li alloys. It has been shown that it is strongly influenced by the type of hardening precipitates and their distribution [11–13]. Hardening precipitates [14–18] and intermetallic particles [14, 19, 20], which are deliberately generated to improve the mechanical properties of alloy, play an important role in pitting corrosion [21–23]. According to Prasad et al. [22], the addition of Cu and Mg to Al–Li binary alloys allows a more varied precipitation. The addition of Cu favors the precipitation of the $\theta(Al_2Cu)$ and $T1(Al_2CuLi)$ phases, while the addition of Mg increases the precipitations of the $S(Al_2CuMg)$ phase. The AA2099 and AA2055 alloys are third-generation Al–Li alloys that are used in the upper and lower wing structures (spars), as well as in fuselage

✉ C. Gaona Tiburcio
citlalli.gaonatbr@uanl.edu.mx

✉ F. Almeraya Calderón
facundo.almerayacld@uanl.edu.mx

[1] FIME-Centro de Investigación e Innovación en Ingeniería Aeronáutica (CIIIA), Universidad Autónoma de Nuevo Léon, Av. Universidad s/n Ciudad Universitaria, San Nicolás de los Garza N. L. 66455, Mexico

[2] División Académica de Ciencias Bilógicas, Universidad Juárez Autónoma de Tabasco, Villahermosa, Tabasco C. P. 86040, Mexico

[3] Facultad de Ingeniería Civil, Universidad Veracruzana, Xalapa 91000, Mexico

Published online: 18 July 2023

structures. They also have applications in aerospace structures (Falcon 9 from the Space X company, and Ares I from NASA) [6, 24, 25].

The AA2055 alloy has a higher density (2.71 g/cm^3) than the AA2099 (2.63 g/cm^3) due to the different Cu/Li ratios of both alloys (1.5 for AA2099 and 3.2 for AA2055) [26, 27]. Compared to the AA2099 alloy, the AA2055 contains a higher Cu content and a lower amount of Li; this causes a higher volume fraction of the T1 phase to develop [26, 28]. Another characteristic of AA2055 is the Ag content of up to 0.7% by weight; this element promotes the formation of the Al_2Cu phase [29, 30]. The addition of Zn (0.3–0.7%) helps to reduce the potential difference between the grain boundaries and the adjacent matrix, as well as to improve the corrosion resistance of the alloy [31].

The precipitates and intermetallic particles developed in Al–Li alloys play an important role in the electrochemical behavior of the alloy. This heterogeneous microstructure also determines the mechanical properties, in such a way that it is important to optimize, by means of thermomechanical treatment, the development and distribution of hardening precipitates [22, 32]

In previous studies, the AA2099-T83 alloy immersed in a 3.5% NaCl solution has been analyzed, where two types of localized corrosion occur, one is due to the distribution of constituent particles of the alloy and the second is directly related with the distribution of grains [33, 34]. It has been recognized that the T1(Al_2CuLi) phase is the predominant phase and is considered the main hardening precipitate, and these are produced during artificial aging at temperatures between 120 and 200 °C. The development of different precipitates with different electrochemical potentials with respect to the matrix depends on the applied thermomechanical treatment. In this way susceptibility to localized corrosion develops.

Jiang et al. [35] studied the effect of different precipitates on the corrosion behavior of an Al–Cu–Li alloy, noting that the corrosion mode changed from intergranular to intragranular as the aging time increased at 160 °C. Peltier et al. [21] examined the way in which corrosion develops in an AA2099-T8 alloy during the early stages of exposure in a NaCl solution. They observed that the first stages of the attack started with the corrosion of the S phase particles (Al_2CuMg), causing dealloying and the formation of cracks around said particles. Lei et al. [36] studied the effect of Li addition and the resulting microstructure on the pitting corrosion behavior of three 2xxx series aluminum alloys. They found that with the increase in Li content, the resistance to pitting corrosion was improved and the passive range was extended. The presence of shallower pits was also observed for samples with higher Li content.

Through an adequate knowledge about the thermomechanical treatments applied to Al–Li alloys and their relationship with the morphology of the microstructure and the precipitates developed, it will be possible to optimize the mechanical properties and the resistance to corrosion of the obtained alloys [37]. In the present work, the corrosion behavior of two third-generation Al–Li alloys AA2099 and AA2055 was evaluated. These alloys were initially subjected to different heat treatments. The electrochemical behavior and mechanical resistance of the alloys under study were investigated as a function of the heat treatment to which they were subjected.

Experimental methodology

Materials

The third-generation Al–Li alloys under study AA2099 and AA2055 were obtained in the form of bars; their nominal chemical composition is shown in Table 1 [38, 39]. These alloys were obtained commercially in T8 heat-treated condition. This consists of a solution treatment (heating to a temperature of approximately 520 °C), followed by rapid cooling (quenching) to retain the Cu in supersaturated solid solution. Subsequently, it undergoes a cold working process, and finally an artificial aging process.

These materials were machined to obtain them in the form of slices 8 cm in diameter and 2 cm thick, for which a silicon carbide disc was used.

Heat treatments

To subject the samples to heat treatments, a Thermolyne, Thermoscientific furnace, was used. A set of samples was subjected to annealing heat treatment. This treatment consisted of bringing the samples up to a temperature of 450 °C. This temperature was maintained for 2 h, to later be allowed to cool in the furnace. Samples subjected to this treatment will be referred to as AA2055-T0 and AA2099-T0. The stages for this treatment are represented in Fig. 1 [40].

Table 1 Chemical composition of the investigated aluminum alloys (w%) [38, 39]

	Li	Cu	Mg	Ag	Zr	Mn	Zn
AA2055	1.15	3.7	0.4	0.4	0.11	0.3	0.5
AA2099	1.8	2.7	0.3	—	0.09	0.3	0.7

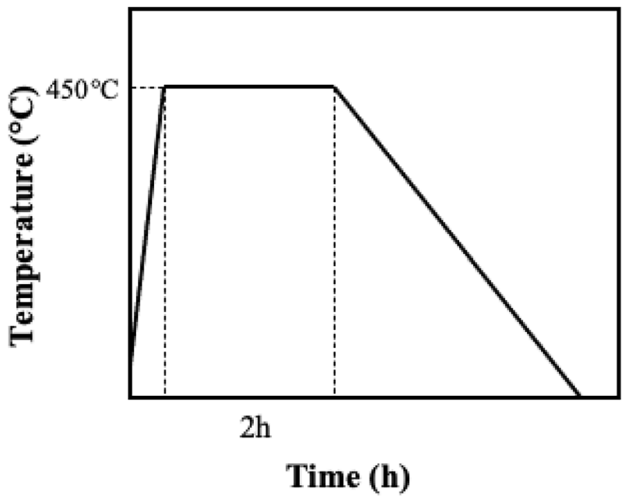

Fig. 1 Stages of the annealing heat treatment

A second group of samples was subjected to a solution treatment at a temperature of 520 °C for 2 h, followed by rapid cooling in water (quenching), then the sample was kept at room temperature (28 °C) for 48 h. An aging process was carried out in two stages, the first of which consisted of raising the temperature of the sample to 150 °C for 24 h, and the second of raising the temperature to 180 °C for 12 h. Finally, the sample was slowly cooled in the furnace. Samples subjected to this treatment will be referred to as AA2055-T6 and AA2099-T6. The stages of this treatment are represented in Fig. 2 [40, 41].

In this way, samples of both alloys were obtained in the three heat treatment conditions, T8 (commercially obtained), T0 (annealed), and T6 (solution treatment and artificial aging).

Microstructural analysis

A set of samples of the alloys, in the three treatment conditions, were prepared metallographically. For this, a successive polishing process was carried out using 600, 800, 1200, 2400, and 4000 grade silicon carbide sandpapers. Subsequently, 1-µm and 1/4-µm diamond paste were successively used to obtain a mirror finish on the samples. The Keller solution (95 mL H_2O, 1.0 mL HF, 2.5 mL HNO_3, 1.5 mL HCl) was used as the etchant for an immersion time of 10 s [42, 43].

A Zeiss metallurgical microscope, Discovery V12 model, was used to analyze the microstructure of the alloys.

The scanning electron microscopy (SEM) technique was also used to observe the microstructure of the samples, obtaining images by backscattered electrons and performing an elemental analysis of the different phases observed by energy dispersive X-ray spectrometry (EDS). A Zeiss Field Emission Scanning Electron Microscopy equipment, model Gemini Sigma 300 VP, was used.

Microhardness tests

Vickers microhardness tests were performed on the different heat-treated samples. For this, a Wilson Hardness model 402MVD microhardness equipment was used, applying a load of 100 g for a time of 10 s. The final microhardness value, for each sample, was obtained by averaging a total of 10 measurements [44].

Electrochemical noise tests

A second set of heat-treated samples was prepared to be subjected to electrochemical noise tests and evaluate the

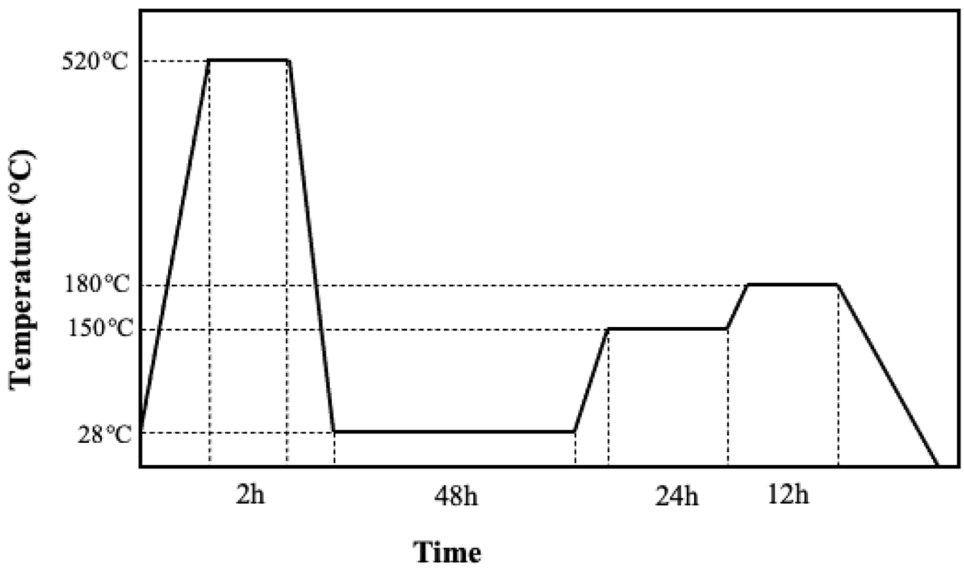

Fig. 2 Stages of solid solution heat treatment and subsequent artificial aging

Table 2 Molarity and pH data of each of the solutions

Solution	Concentration	Molarity	pH
NaCl	3.5% weight	0.0599 mol/lt	7
HCl	1% volume	0.326 mol/lt	0.487
H_2SO_4	1% volume	0.186 mol/lt	0.723

corrosion performance of each of the alloys. For these tests, the samples were successively roughened to 600 grade sandpaper, rinsed and dried with alcohol and compressed air, then left to rest for 24 h in a desiccator to ensure the formation of the passive layer. A potentisotat/galvanostat/ZRA Gill ACM Instruments equipment was used. These tests were based on the ASTM-G199 standard [45].

An electrochemical cell with a three-electrode system was also used, two nominally identical working electrodes made up of the aluminum alloy samples and a saturated calomel reference electrode (SCE).

Simultaneous measurement of electrochemical noise in current and potential was performed. Current electrochemical noise measurements were made between the two working electrodes, while potential electrochemical noise measurements were made between one of the working electrodes and the reference electrode. Electrochemical noise tests were performed in 3.5% by weight NaCl, 1% by volume HCl, and 1% by volume H_2SO_4 solutions. Table 2 shows the molarity and pH data of the solutions before carrying out the test.

For the preparation of these solutions, commercial reagents were used, with the characteristics shown in Table 3.

The exposure area of the samples was 1 cm^2. Noise tests were performed at a rate of 1 data per second and a total of 2048 data per test were recorded. The time series obtained from the electrochemical noise tests were visually analyzed. In order to obtain stationary recordings, the direct current DC tendency of the signals was then removed using a MATLAB software using the polynomial approach. Statistical characteristics including the location index (LI), skew, and kurtosis were obtained after the DC trend was taken into account. These parameters may help identify the kind of corrosion that take place.

An analysis in the frequency domain was also carried out by means of spectral power density plots, which offer information about the corrosion mechanism present through parameters such as the zero-limit frequency ψ^0 and the slope β.

Table 3 Characteristics of the reagents used

Reagent	Mark	Purity	Density
NaCl	Chemika	99.8%	2.17 g/mL
HCl	Wohler	37.25%	1.19 g/mL
H_2SO_4	Wohler	96.5%	1.83 g/mL

Results and discussion

Microstructural analysis

Figure 3a–c present the images of the microstructures of the AA2099 alloy, in the three heat treatment conditions, obtained by SEM with their corresponding elemental microanalysis. In T0 condition, a surface of clearly defined grains is observed, with equiaxed morphology, whose diameters are homogeneously distributed. This grain distribution is the result of the recrystallization process during the annealing heat treatment. In the T6 heat-treatment condition, defined grains are similarly observed, whose morphology is less uniform than in the previous case. Precipitation is observed at the grain boundaries, product of the aging of supersaturated solid solution. Most of the precipitated particles occur at grain boundaries. It is known that the hardening phases preferentially precipitate in crystallographic defects, with dislocations and grain boundaries [46, 47]. Larger intermetallic particles are also observed, whose diameters range between 5 and 10 μm and with significant Cu and Fe contents. In the T8 heat-treatment condition, deformed grains are observed, a product of cold working, as well as precipitated particles at the grain boundaries and inside the grains (in light tones). As was already indicated, cold deformation causes dislocations to occur inside grains which act as a preferred place for the nucleation of hardening precipitates, causing them to form outside grain borders, or in the matrix. The composition of the matrix is high in Al content, around 95% by weight, and Cu, around 2.6% by weight. The contents of Mg and Zn in the matrix are around 0.9 and 0.6% by weight, while the rest of the elements such as Si and Mn appear in amounts less than 0.5% by weight.

Figure 4a−c present the images of the microstructures of the AA2055 alloy, in the three heat-treatment conditions, obtained by SEM with their corresponding elemental microanalysis. In T0 condition, a high number of elongated precipitates is observed, whose Cu content is relatively high (around 22% by weight). These particles extend along the grain boundaries. The presence of precipitation free zones is also observed in the regions adjacent to the grain boundaries. This microstructure is the result of the higher Cu and Ag contents in this alloy, compared to AA2099. The Ag element, as already established, encourages the emergence of secondary phases in the alloy. During the recrystallization phase, areas without precipitation emerge. A surface with less precipitated particles is seen in the T6 heat-treatment condition, which may be related to the solid-solution treatment. Near the grain boundaries, the majority of the precipitates formed. Additionally, fissures were shown to form, which was most likely caused by temperature differences between the alloy's inside and exterior that emerged during the alloy's quenching process. In the T8 heat-treatment condition, a uniform

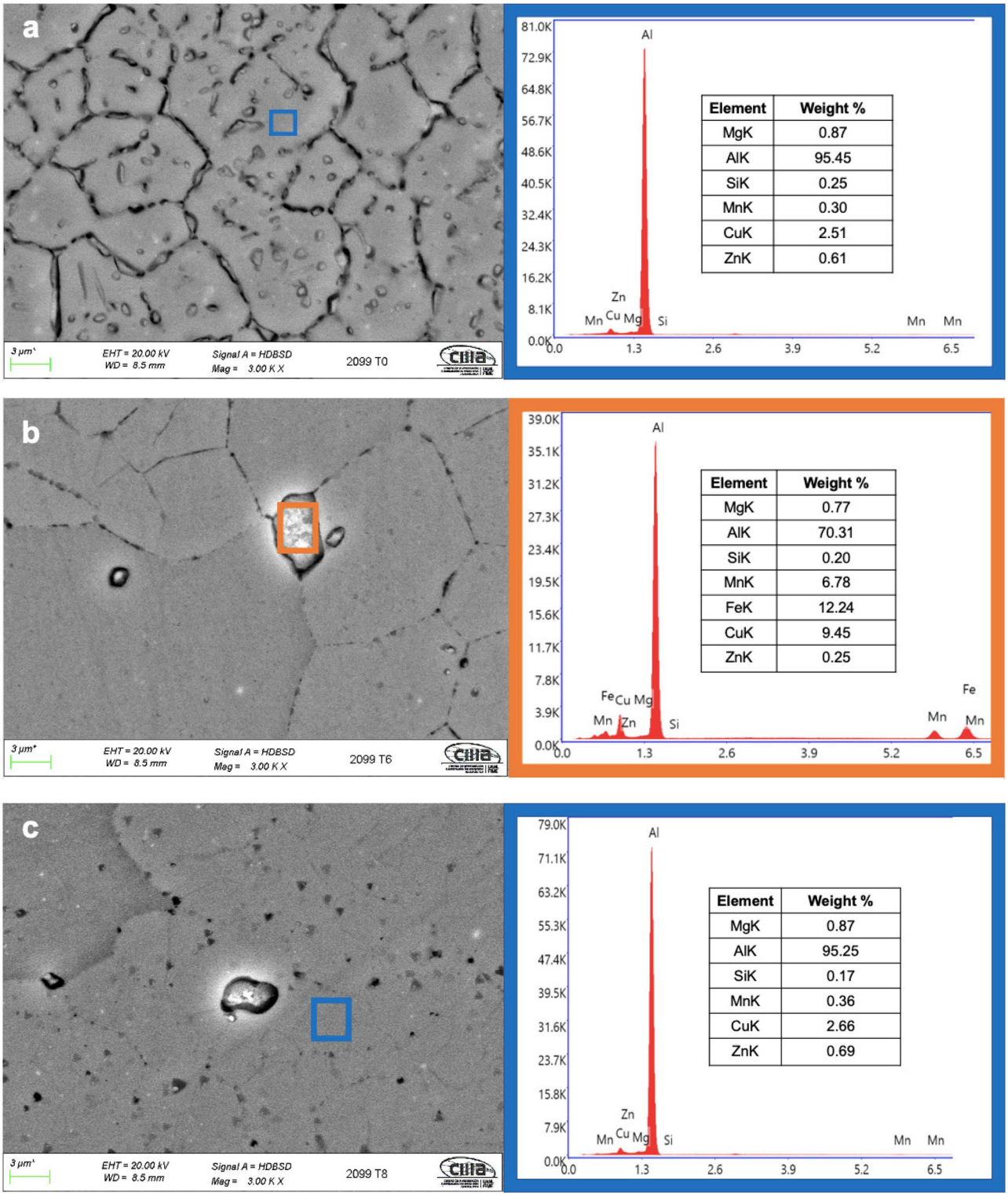

Fig. 3 SEM-EDS surface micrographs of AA2099 alloy under **a** T0, **b** T6, and **c** T8 heat-treatment conditions

distribution of deformed grains is observed in the extrusion direction. Some precipitated phases (in light tones) are also observed, similarly oriented in the direction of cold working. Additionally, a regular distribution of dark dots is seen; these could be holes made when precipitated particles were removed during mechanical polishing.

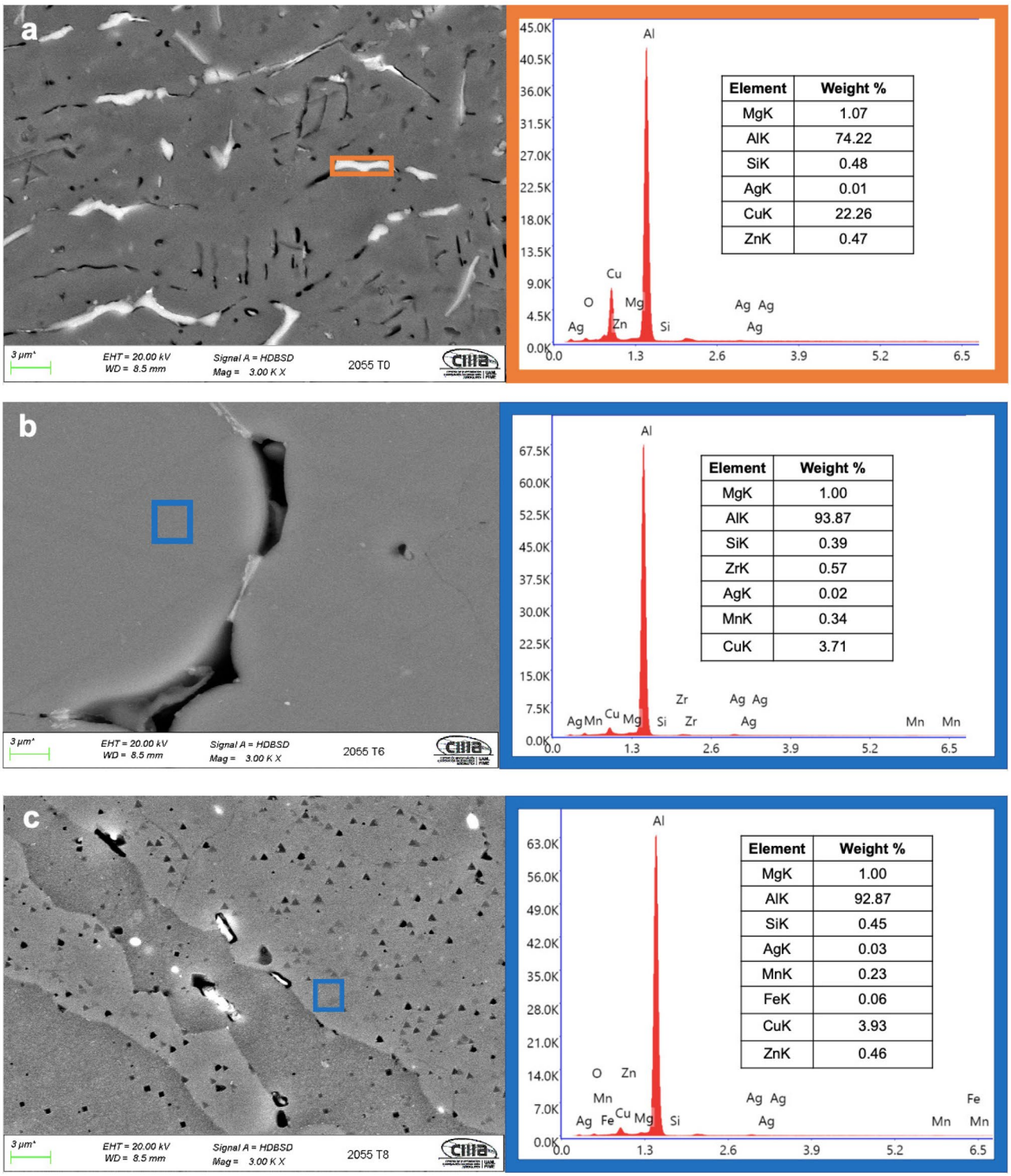

Fig. 4 SEM-EDS surface micrographs of AA2055 alloy under **a** T0, **b** T6, and **c** T8 heat treatment conditions

The matrix of the AA2055 alloy contains, in general, more than 93% by weight of Al and about 4% by weight of Cu. The Mg content is also important, around 1%. The rest of the alloying elements, such as Si, Ag, Mn, and Zn, appear in quantities of less than 0.5%.

Microhardness results

Figure 5 shows the results of the microhardness tests of the alloys. As expected for this heat treatments, it is seen that the alloys in T0 condition have the lowest microhardness

values for both alloys (HV 62.3 for AA2099 and HV 77.8 for AA2055). This is because annealing causes dislocations to move, which removes internal stresses in the material and lowers its hardness while increasing its ductility [48, 49].

The production of hardening precipitates during solid solution treatment, quenching, and artificial aging results in an increase in microhardness for alloys in the T6 condition (HV 164.28 for AA2099 and HV 174.78 for AA2055). These precipitates make the alloy harder by preventing dislocations from moving. The T8 condition yielded the greatest microhardness values (HV 177.32 for AA2099 and 199.44 for AA2055), which may be attributed to the use of cold working in this condition to create dislocations inside the grains. As dislocations are preferred precipitate nucleation sites, hardening precipitates are produced both within and outside of the grains during this heat-treatment condition. This can be observed in the SEM images than for alloys in T8 condition, in which there is a greater amount of precipitates distributed throughout the surface of the alloy; they can even be observed inside the grains. The AA2055 alloy presented higher microhardness values, with respect to AA2099, regardless of the heat treatment performed. This can be attributed to the content of the Ag element in AA2055, which, as mentioned by Zhou et al. [29], as well as Bai et al. [30], promotes the formation of omega phases (Al_2Cu) in Al–Cu–Mg alloys. Furthermore, it has been widely reported that Ag additions promote a higher volume fraction and uniform nucleation of T1 precipitates in Al–Cu–Li alloys, particularly when combined with Mg. It has also been reported that both Ag and Mg decrease the fault-stacking energy of the alloy, which causes dislocation mobility to be reduced [50–53].

Electrochemical noise (EN)

Figure 6 shows the time series, in potential and current, obtained from the electrochemical noise tests, for both alloys in the three heat-treatment conditions, T0, T6, and T8, in the presence of 3.5% NaCl. It is observed (Fig. 6a) that the AA2055 alloys in the three heat-treatment conditions present a tendency toward active potentials throughout the test. The AA2055-T6 alloy presents transients of approximately 7 mV amplitude; this from beginning of the test until approximately 700 s; after this time the amplitude of the transients decreases noticeably. This will be related to the presence of initial pitting and re-passivation of the surface over time.

The AA2099 alloy in T6 and T8 conditions does not present visible potential transients; only in the case of the AA2099-T0 alloy it presents transients of approximately constant amplitude, during the entire test and almost zero DC trend. Such a behavior, and due to the shape of the fluctuations, seems to correspond to uniform corrosion activity. In the current time series (Fig. 6b), there is some correspondence with the potential time series since the AA2055-T6 and AA2099-T0 alloys present fluctuations in current, while the AA2099 alloys in T6 and T8 conditions do not present visible transients. It can be said that in the presence of NaCl, the alloys with the highest corrosive activity are AA2055-T0, AA2055-T6, and 2099-T0. In the case of AA2055-T0, this result may be related to the high number of precipitates present in the microstructure. As for the AA2055T6 alloy, it can be related to the precipitates at the grain boundaries and the developed cracks.

Samaniego-Gámez et al. [54] points out that impurities present on the surface of an AA2055 alloy affect the

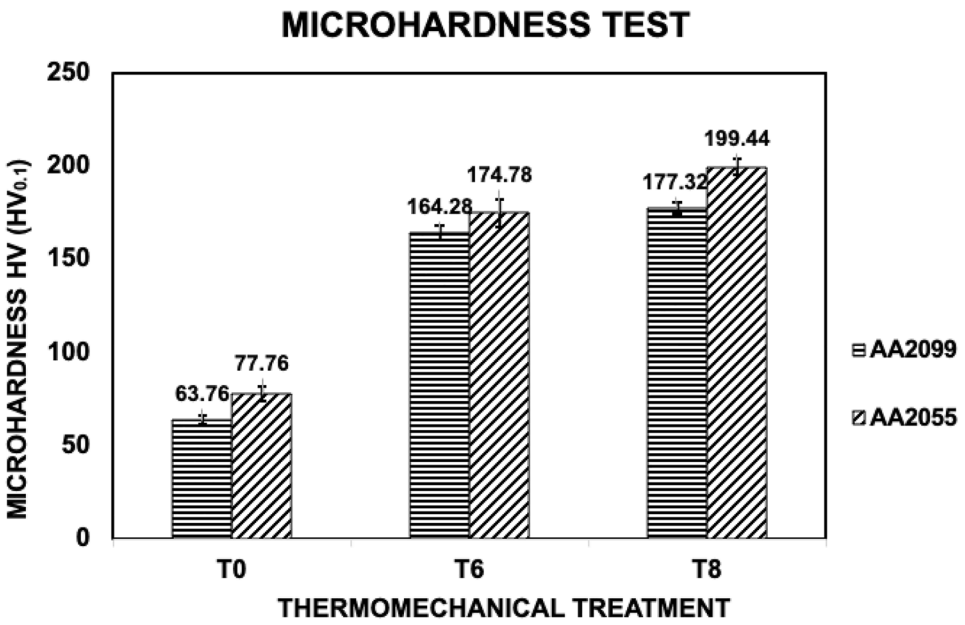

Fig. 5 Microhardness test results graph

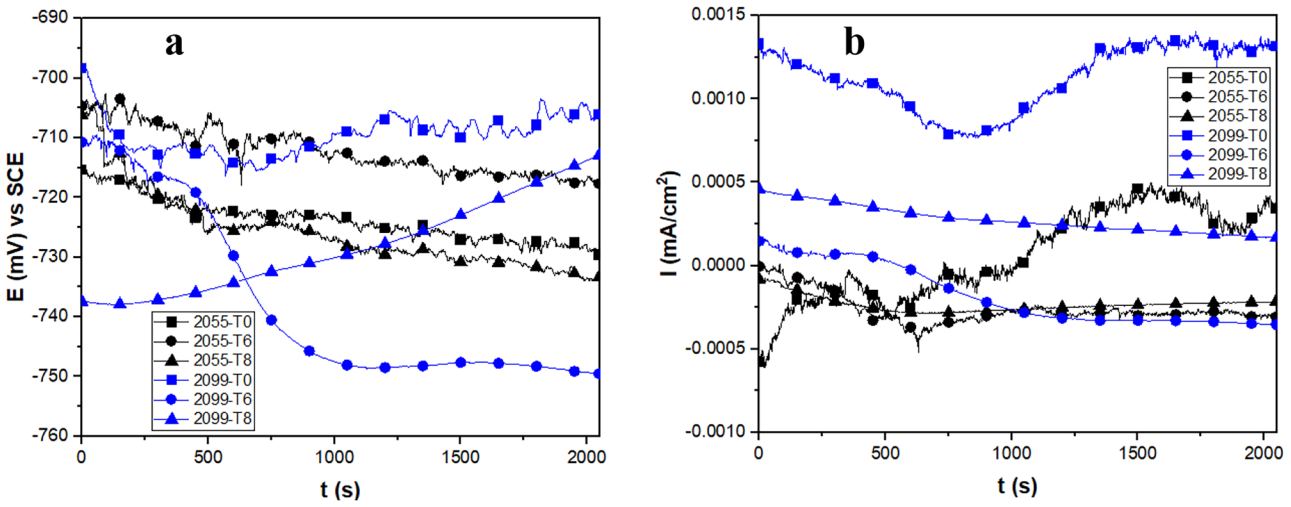

Fig. 6 Time series **a** in potential and **b** in current, for alloys AA2055 and AA2099 in the three heat-treatment conditions, in the presence of 3.5 wt.% NaCl

homogeneity of the passive layer of the alloy, decreasing the resistance to localized corrosion. During the annealing heat treatment, the solute elements precipitate in the form of second phases, mainly Al_2Cu, Al_2CuLi, and intermetallic particles. It has been widely documented that this precipitation occurs mainly at grain boundaries [52, 53]. Similarly, it can be deduced that the high number of second phase particles observed in these alloys, as well as the cracks developed in AA2055-T6, may be developing a deficient passive film that is easily attacked and destroyed locally by aggressive ions with Cl^-.

As background, it can be mentioned that Ju et al. [55] investigated the development of pitting corrosion in an AA2024 alloy when immersed in 0.35wt.% NaCl and 3.5wt.% NaCl solutions. They observed that the concentration of Cl^- ions increases pitting formation and hydrogen evolution in Al, that is, the higher the concentration of Cl^- ions, the more serious the destruction of the passivation film on the surface. Much lower corrosion potentials were found for the alloy immersed in 3.5wt.% NaCl than for the alloy in 0.35wt.% NaCl.

Figure 7 shows the time series obtained for both alloys in the three heat-treatment conditions, in the presence of 1 wt.% HCl. It is observed (Fig. 7a) that the AA2099-T6 alloy starts from noble potentials and presents a clear trend toward active potentials. Furthermore, this alloy exhibits potential transients at the beginning of the test that get smaller with time. This phenomenon could be related to the repassivation of the surface of the material. The rest of the alloys present behaviors that consist of an almost null DC tendency, that is, they do not exhibit appreciable behaviors toward active potentials or noble potentials. The AA2055-T0 alloy presents the most active potential values, while the AA2099-T0 and AA2055-T6 alloys present the noblest potentials and very similar behaviors. In the same way, the alloys AA2099-T8 and AA2055-T8 present a very similar behavior. In the current time series (Fig. 7b), no notable transients are observed, so a trend toward an increase in system current demand can only be mentioned for the AA2099-T8 and AA2055-T0 alloys. Although it seems that, according to this visual analysis, the alloys with the greatest susceptibility to corrosion are AA2099-T6 and AA2055-T0, it should be noted that these time series present, in general, nobler potentials than those corresponding to the NaCl solution at 3.5wt.%, so there is less aggressiveness in the HCl solution. This can be attributed to a lower release of Cl^- ions, or to the lower concentration of these ions, in this solution. The HCl solution is present in a lower concentration than the NaCl solution. It is a possible cause of the lower release of Cl^- ions. On the other hand, the NaCl solution contains Na^+ and Cl^- ions that dissociate with relative ease from polar water molecules. This suggests better ion release in aqueous solution. On the other hand, the susceptibility to corrosion shown by the AA2099-T6 alloy coincides with what was observed by Ma et al. [56] when analyzing potentiodynamic polarization curves of AA2099 alloy samples immersed in 3.5 wt.% NaCl. They observed that the alloy in T6 condition experienced a shift in potential toward a more negative direction than in other treatment conditions such as T3 and solution treatment.

Figure 8 shows the current and potential time series of both alloys in the three heat-treatment conditions in the presence of H_2SO_4. It is observed that in the potential noise signal (Fig. 8a), all the alloys present a similar behavior presenting a clear DC trend toward active potentials. Only in the case of the AA2099-T0 alloy, modest amplitude fluctuations first occur at the beginning of the

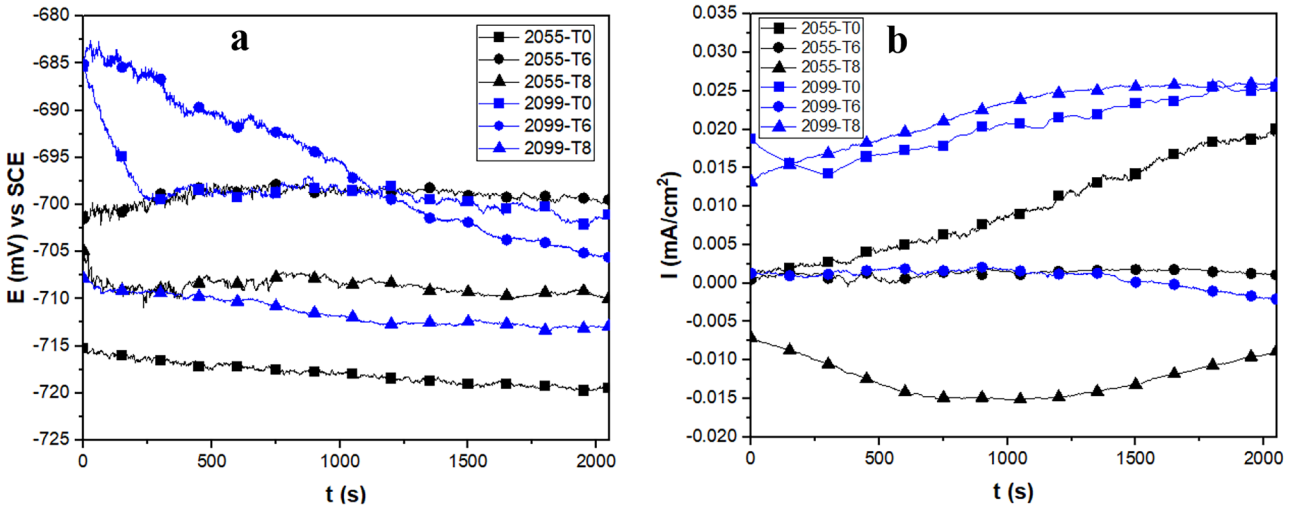

Fig. 7 Time series **a** in potential and **b** in current, for alloys AA2055 and AA2099 in the three heat-treatment conditions, in the presence of 1 wt.% HCl

test and then disappear in the smooth curves of these signals. Similar smooth curves are shown in the current noise signals (Fig. 8b), with no transients and similar DC trends for most alloys, except for AA2099-T0, which has a trend toward higher current demand. This behavior could be attributed to a permanent passive state of the alloys in the presence of 1 wt.% H_2SO_4. It is likely that the absence of Cl^- ions and the low acid concentration are the causes, as mentioned by Gaona et al. [57, 58] when studying localized corrosion in Ni-based superalloys at room temperature using electrochemical noise in 10% wt.% H_2SO_4 and CH_3COOH solutions.

Analysis by means of statistical parameters

The results of the noise tests were also analyzed by means of the determination of statistical parameters that provide information about the electrochemical processes that occur in the alloys during the test. To carry out this analysis, it was necessary to eliminate the DC trend of the noise signals and thus obtain stationary records that improve the reliability of the analysis of statistical parameters [59–61].

One of the statistical parameters used is the standard deviation σ that allows evaluating the dispersion of a data set with respect to the mean value. Its application can be

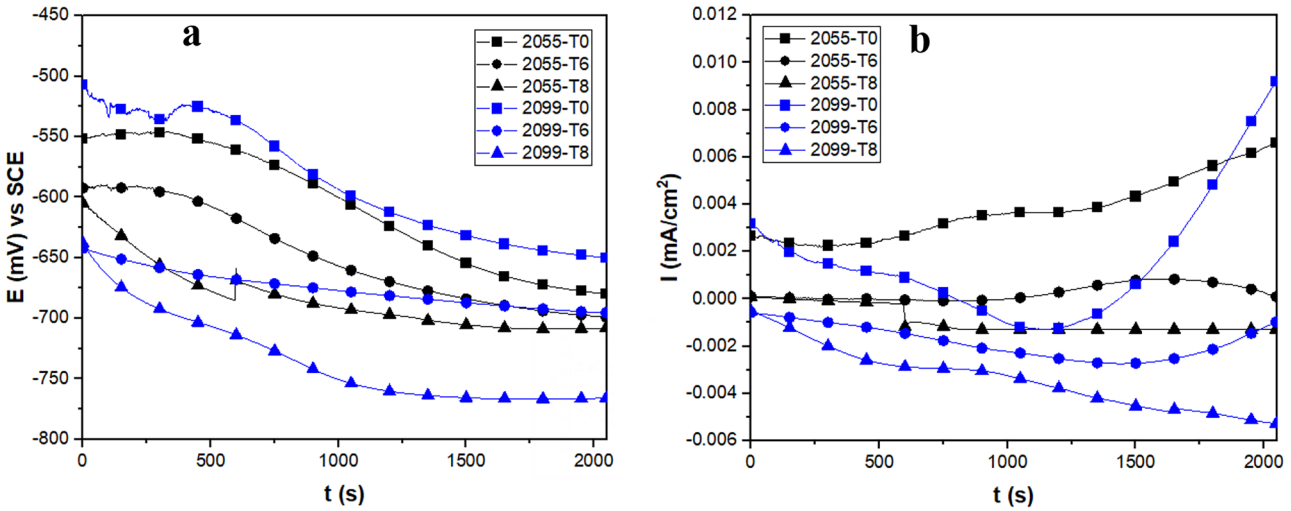

Fig. 8 Time series **a** in potential and **b** in current, for alloys AA2055 and AA2099 in the three heat-treatment conditions, in the presence of 1wt.% H_2SO_4

very useful to quantify the amplitude of the fluctuations. It is defined as the square root of the variance (Eq. 1) [62].

$$\sigma = \sqrt{x_{\sigma^2}} \tag{1}$$

Being x_{σ^2} the variance calculated by means of Eq. (2):

$$x_{\sigma^2} = \frac{\sum_{n=1}^{N} \left(x_n - \bar{x}\right)^2}{N - 1} \tag{2}$$

The use of the standard deviations of the potential, σ_v, and current intensity, σ_i for the interpretation of the noise records can be done through their relationship, called resistance to noise Rn, which is calculated by the relationship between the standard deviations of the records of potential and current intensity (Eq. 3) [63].

$$Rn = \left[\frac{\sigma_v}{\sigma_i}\right] * A \tag{3}$$

By comparing the average current value to the size of the variations, the localization index (*LI*) makes it easier to distinguish between localized and uniform corrosion process. Given that the current flows between the two working electrodes in either direction, the localization index is calculated using the root mean square of the current (Eq. 4) [64, 65].

$$LI = \frac{\sigma_i}{i\sqrt{\bar{x}^2}} = \sqrt{\frac{\sum_{n=1}^{N} \left(i_n - \bar{i}\right)^2}{\sum_{n=1}^{N} \left(i_n\right)^2}} \tag{4}$$

The localization index is bounded between the values 0 and 1. The *LI* value is used to classify the process that is taking place according to Table 4.

As an alternative to the previous parameters, the skewness (x_σ^3) is used to measure the symmetry of the signal and the kurtosis (x_σ^4) to detect changes in the distribution of its values. These values are calculated using Eqs. (5) (skewness) and (6) (kurtosis) [65–67]:

$$x_{\sigma^3} = \frac{\sum_{n=1}^{N} \left(x_n - \bar{x}\right)^3}{(N - 1)\sigma^3} \tag{5}$$

$$x_{\sigma^4} = \frac{\sum_{n=1}^{N} \left(x_n - \bar{x}\right)^4}{(N - 1)\sigma^4} \tag{6}$$

Table 4 Type of corrosion process depending on the localization index (*LI*)

Corrosion type	*LI*
Localized	1.0–0.1
Mixed	0.1–0.01
Uniform	0.01–0.001

The above values are moments of the series. In this way x_σ^2 is the second moment of the temporal register, that is, the variance; x_σ^3 the third (the skewness); and x_σ^4, the fourth (the kurtosis).

The determination of these statistical parameters generates a standard error in the results. This standard error is given by Eq. (7) [67, 68]:

$$SE = \sqrt{\frac{24}{N}} \tag{7}$$

where N is the number of data studied in the electrochemical noise technique.

In the present study $SE = 0.108$.

The type of corrosion determined by kurtosis and skewness is given by Table 5 [69–71].

Table 6 summarizes the values of the statistical parameters that were obtained from the electrochemical noise tests, for the three alloys, in the three heat-treatment conditions, and in the presence of the three electrolytes. It can be noted that in the presence of 3.5 wt.% NaCl, the statistical parameters indicate the same types of corrosion for four of the alloys: AA2099-T0, AA2099-T6, AA2055-T6, and AA2055-T8. For these four alloys, LI indicates mixed corrosion, kurtosis indicates pitting corrosion, and skew indicates uniform corrosion. According to what was observed in the visual analysis, it could be a tendency toward uniform corrosion due to the large number of transients of low amplitude and high frequency (Fig. 6), except in the case of the AA2099-T6 alloy, whose signal, both in current as in potential, they are devoid of transients and could be in a passive state during the test. The AA2099-T8 alloy similarly presents signs in the form of a smooth curve, so the result of parameters that indicate uniform corrosion is reasonable. The AA2055-T0 alloy indicates localized corrosion for LI, pitting for kurtosis, and uniform corrosion for skew. Pitting corrosion could be assumed for this alloy if the transients observed in the visual analysis of Fig. 6 are considered, especially in the current noise signal. Consequently, it is assumed that in the presence of NaCl, the AA2055-T0 alloy presents greater susceptibility to corrosion, while the alloys that present greater resistance to corrosion are the AA2099-T8 and AA2099-T6

Table 5 Type of corrosion as a function of skew and kurtosis values

Corrosion type	Potential		Current	
	Skewness	Kurtosis	Skewness	Kurtosis
Uniform	$< \pm 1$	< 3	$< \pm 1$	< 3
Pitting	< -2	$\gg 3$	$> \pm 2$	$\gg 3$
Transgranular (SCC)	4	20	−4	20
Intergranular (SCC 1)	−6.6	18 a 114	1.5 a 3.2	6.4 a 15.6
Intergranular (SCC 2)	−2 a −6	5 a 45	3 a 6	10 a 60

Table 6 Type of corrosion as a function of skew and kurtosis values

Solutions	Materials	Heat treatment condition	Rn (ohm)	I_{corr} (mA/cm^2)	LI	Corrosion type	Kurtosis (I)	Corrosion type	Skew (*I*)	Corrosion type
NaCl	AA2099	T0	4.21×10^4	6.17×10^{-4}	0.020	Mix	4.2	Pitting	−0.3	Uniform
		T6	1.37×10^5	1.90×10^{-4}	0.019	Mix	13	Pitting	−0.2	Uniform
		T8	5.34×10^4	4.86×10^{-4}	0.002	Uniform	4.9	Pitting	−0.2	Uniform
	AA2055	T0	1.09×10^4	2.38×10^{-3}	0.167	Localized	3.1	Pitting	0.2	Uniform
		T6	5.59×10^4	4.64×10^{-4}	0.065	Mix	8.1	Pitting	−0.8	Uniform
		T8	2.72×10^5	9.57×10^{-5}	0.013	Mix	8.1	Pitting	0.9	Uniform
HCl	AA2099	T0	1.16×10^3	2.24×10^{-2}	0.018	Mix	3.1	Pitting	0.01	Uniform
		T6	1.83×10^3	1.41×10^{-2}	0.150	Localized	3.0	Pitting	−0.3	Uniform
		T8	1.17×10^3	2.22×10^{-2}	0.0.005	Uniform	3.0	Pitting	−0.3	Uniform
	AA2055	T0	5.47×10^2	4.74×10^{-2}	0.027	Mix	3.8	Pitting	−0.3	Uniform
		T6	1.37×10^3	1.89×10^{-2}	0.151	Localized	7.3	Pitting	0.3	Uniform
		T8	4.16×10^3	6.26×10^{-3}	0.006	Uniform	2.8	Uniform	−0.3	Uniform
H_2SO_4	AA2099	T0	5.51×10^4	4.71×10^{-4}	0.009	Uniform	4.9	Pitting	0.6	Uniform
		T6	5.49×10^3	4.73×10^{-3}	0.006	Uniform	2.6	Uniform	−0.02	Uniform
		T8	1.38×10^4	1.89×10^{-3}	0.005	Uniform	6.4	Pitting	−1.0	Uniform
	AA2055	T0	1.43×10^4	1.82×10^{-3}	0.006	Uniform	3.6	Pitting	0.1	Uniform
		T6	5.81×10^4	4.47×10^{-4}	0.017	Mix	4.9	Pitting	−0.3	Uniform
		T8	2.27×10^4	1.14×10^{-3}	0.087	Mix	11	Pitting	0.07	Uniform

alloys, apparently, they remain in a passive state. The rest of the alloys may be presenting uniform corrosion, according to what is indicated by the statistical parameters and the analysis of the noise signals. In the presence of HCl, the statistical parameters indicate greater susceptibility to corrosion for alloys AA2099-T6 and AA2055-T6 since kurtosis and LI indicate localized corrosion, while for alloys AA2099-T8 and AA2055-T8, there is less susceptibility to corrosion by indicating uniform corrosion for LI and skew; in addition, the noise signals for these alloys (Fig. 7) do not present significant transients. For the other two alloys, it could be mixed corrosion with some pitting, as indicated by the statistical parameters and the noise signals in potential and current (Fig. 7) that presented frequent low-amplitude fluctuations. In the presence of H_2SO_4, all the alloys could be presenting uniform corrosion, as indicated by the statistical parameters; even some of the alloys could have remained in a passive state during the test, according to the noise signals in Fig. 8.

In general, the apparently poor relationship between the results obtained by the statistical parameters can be attributed to the density of pits formed on the surface of the material. In other words, if the pitting density is high, the skew parameter could be attributed to a uniform type of corrosion.

Power spectral density (frequency domain)

The study of the corrosion processes that occur at the metal-electrolyte interface was also carried out through an analysis in the frequency domain through power spectral density (PSD) signals. The results obtained in this analysis will be compared with the corresponding ones in the analysis of statistical parameters.

During the analysis of PSD signals, three important parameters are defined: the slope of the high-frequency linear zone β, the value of the power at the zero-frequency limit ψ^0, and the cut-off frequency that separates the high-frequency zones and low frequencies f_c. These parameters have been related to the mechanisms and rates of corrosion present [72, 73].

The information obtained from electrochemical noise tests in the time domain can be transformed into noise signals as a function of frequency by applying the fast Fourier transform (FFT) to the data using Eqs. (8) and (9) [74].

$$R_{xx} = \frac{1}{N}\sum_{n=0}^{N-m+1} x(n)\cdot x(n+m) \quad when\ values\ are\ from\ 0 < n < N \tag{8}$$

$$\psi_x(k) = \frac{\Upsilon \cdot t_m}{N}\cdot \sum_{n=1}^{N}\left(x_n - \overline{x_n}\right)\cdot e^{\frac{-2\pi k n^2}{N}} \tag{9}$$

The slope is used to find the corrosion mechanism. The value of the slope is based on the cutoff frequency, i.e., the point where the slope begins. The slope is defined by β_x and is represented by Eq. (10):

$$\log \psi_x = -\beta_x \log f \tag{10}$$

The PSD signals are related to the total energy present in the system. So, the zero limit frequency provides information about the dissolution of the material [65, 75]. The dissolution of the material occurs only in the current PSD. Table 7, proposed by Mansfeld et al., determines the corrosion phenomena that occur on the surface of AA 2024-T0 [72, 75].

Figure 9 shows the current PSD graphs for the two alloys under study, under the three heat treatment conditions, in the presence of 3.5 wt. % NaCl solution, dBi as a function of frequency f(Hz). The value of the slope (β) in current is related to the corrosion mechanism. In this exposure environment, both alloys presented very similar values of the zero limit frequency (ψ^0) regardless of the heat treatment condition, which indicates similar corrosion or dissolution kinetics of the material for both alloys. Very similar behaviors are also observed at high frequencies for the alloys in T0 condition, whereas in T6 and T8 conditions, the AA2055 alloy presented higher dB values. A very low slope is also observed in T8 condition for both alloys. Based on what was observed in these PSD signals, it can be deduced that in conditions T0 and T6, there is greater electrochemical activity, since there are higher values of ψ^0 and dB than in condition T8. In addition, it is observed that in T8 condition, the lowest values of the β slope are presented, indicating less electrochemical activity. This largely coincides with what was observed in the visual analysis of the time series and was related to the distribution of precipitates and intermetallic particles on the alloy surface at T0 and T6 conditions, as well as the high concentration of chloride ions in the alloy electrolyte.

Figure 10 shows the current PSD graphs for the two alloys under study, under the three heat-treatment conditions, in the presence of 1 wt. % HCl solution, dBi as a function of frequency f(Hz). It is observed that in conditions T0 and T6, very similar and higher dB values are presented than the values that are presented with condition T8. For conditions T0

Table 7 β intervals to indicate the type of corrosion

Corrosion type	dB (V) · decade^{-1}		dB (A) · decade^{-1}	
	Minimum	Maximum	Minimum	Maximum
Uniform	0	−7	0	−7
Pitting	−20	−25	−7	−14
Passive	−15	−25	−1	1

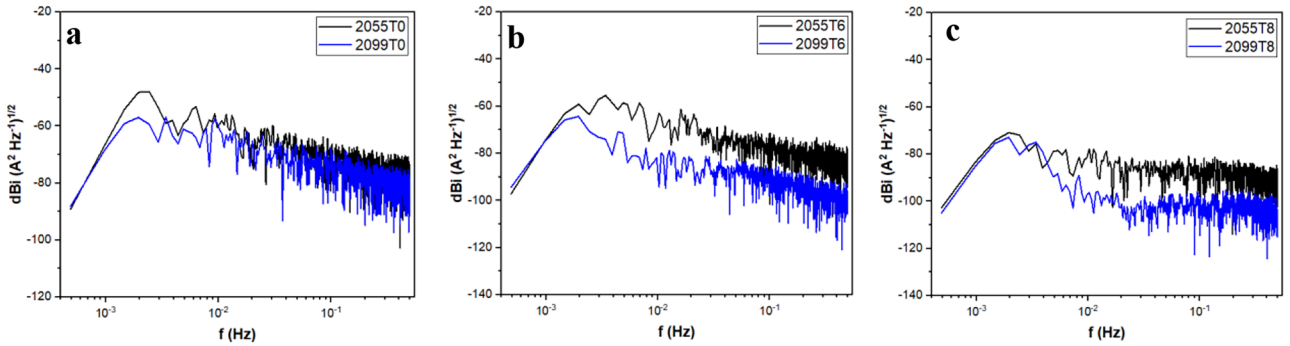

Fig. 9 Power spectral density (PSD) in current, for aluminum alloys in **a** T0, **b** T6, and **c** T8 heat-treatment condition, exposed in a 3.5 wt. % NaCl solution

and T6, both the zero limit frequency ψ^0 and the dB value at the cutoff frequency are very similar in both alloys. It is also observed that in T0 condition and at high frequencies, the AA2055 alloy presents higher dB values than the AA2099. In T6 condition, both alloys present very similar conditions at low frequencies and at high frequencies. In T8 condition, the dB values are lower; in addition, the behavior of the signals for both alloys is very similar, both at low frequencies and at high frequencies. It can be affirmed that, according to the above, there is greater electrochemical activity in conditions T0 and T6, while in condition T8 the resistance to corrosion is greater. In particular, in T0 condition, the AA2055 alloy presents greater susceptibility to corrosion than the AA2099.

Figure 11 shows the current PSD graphs for the two alloys under study, under the three heat-treatment conditions, in the presence of 1 wt. % H2SO4 solution, dBi as a function of frequency f(Hz). In this case it is observed that in condition T0, the PSD signals present very similar behaviors. Both the values of ψ^0, the value of dB at the cutoff frequency, and the slope are quite similar in both signals. In T6 condition, the AA2099 alloy presents a higher value of ψ^0, indicating greater dissolution of the material; however, at high frequencies the dB values in this alloy become lower than those corresponding to AA2055. In T8 condition, the AA2055 alloy does not present appreciable fluctuations; the PSD signal has the form of a soft cure, both at low frequencies and at high frequencies, even the AA2099 alloy in the same T8 condition presents few fluctuations at low frequencies, which is they intensify at high frequencies, that is, they present fewer fluctuations than in the rest of the signals. This could indicate that both alloys may be remaining in a passive state. It can be deduced that in the presence of H_2SO_4, both alloys present greater resistance to corrosion when they are fired in the T8 heat-treatment condition.

Table 8 summarizes the values of the PSD parameters obtained. It is observed that in the presence of NaCl, the current slope values indicate pitting corrosion for the alloys AA2099-T0, AA2099-T6, AA2055-T0, and AA2055-T6, while for the alloys AA299-T8 and AA2055-T8, it indicated uniform corrosion, which coincides with what was observed in the analysis of statistical parameters (Table 4) and confirms the good resistance to corrosion of the alloys in T8 condition.

In the presence of HCl it is observed that all the values of the slopes indicate pitting corrosion for all the alloys. In the

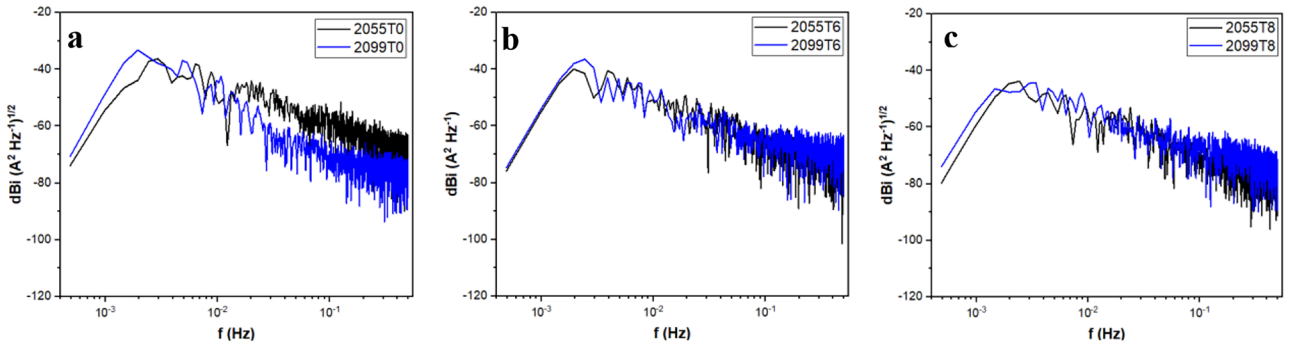

Fig. 10 Power spectral density (PSD) in current, for aluminum alloys in **a** T0, **b** T6, and **c** T8 heat-treatment condition, exposed in a 1% wt HCl solution

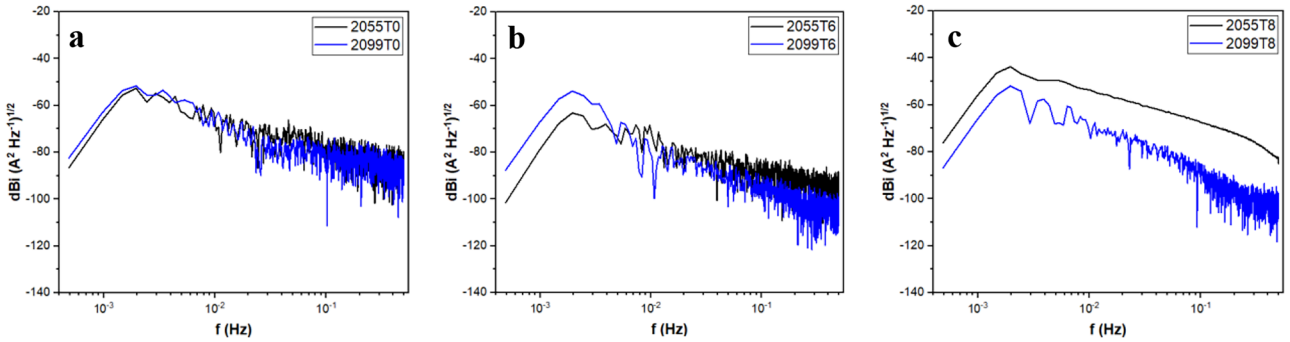

Fig. 11 Power spectral density (PSD) in current, for aluminum alloys in **a** T0, **b** T6, and **c** T8 heat-treatment condition, exposed in a 1% wt H_2SO_4 solution

analysis of statistical parameters, a greater susceptibility to localized corrosion was deduced for the alloys AA2099-T6 and AA2055-T6. Then such a statement can be sustained if it is considered that the rest of the alloys have a large amount of pitting to be considered generalized corrosion.

In the presence of H_2SO_4, all the values of the slopes indicate pitting corrosion, being able to deduce the same situation as in the previous case. The amount of pitting is so high that general corrosion can be considered.

The alloys that presented greater susceptibility to corrosion were AA2055-T0, AA2055-T6,and AA2099-T6, especially in the presence of solutions containing Cl^- ions. The AA2055-T0 alloy presented a high number of precipitates in its microstructure, while the AA2055-T6 presented a development of cracks at the grain boundaries; this can be observed in Fig. 5a, b. These factors influence the development of localized corrosion of alloys. In the case of the AA2099-T6 alloy, after solution treatment and artificial aging, precipitates developed at the grain boundaries that could be forming galvanic pairs with the surrounding matrix. Buchheit et al. [16, 76, 77] have extensively documented that the T1(Al_2CuLi) phase is the main cause of grain/subgrain boundary attack. It is possible to notice the development of precipitated phases in the SEM images (Fig. 4) that probably correspond to this T1 phase. As mentioned by Li et al. [13], at the beginning of the pitting process, this phase is anodic with respect to the matrix, to later become cathodic because of the preferential dissolution of Al and Li of the T1 phase. The preferential precipitation of the T1 phase in crystallographic defects such as grain/subgrain boundaries is one of the factors that significantly influence the development of localized corrosion, as well as chloride-containing environments. Similarly, the dissolution of Cu-depleted zones that form adjacent to the grain and subgrain boundaries, due to the local precipitation of Cu-rich phases, can be associated with intergranular attack, as previously reported [78].

The AA2099-T0 alloy presented a microstructure with few precipitated particles. As these Cu-rich phases do not occur, differences between surface potentials do not develop, so that galvanic pairs in the microstructure are scarce. The AA2099-T8 alloy may be presenting a better distribution of precipitates in the microstructure, since cold deformation causes dislocations to form inside the grains, in such a way that the precipitates develop throughout the matrix instead of do it only at grain boundaries. Cold deformation also causes the widening of the Cu scarcity zones to decrease, thus decreasing the susceptibility to localized corrosion. This phenomenon can also be related to the better corrosion performance of the AA2055-T8 alloy, apart from the fact that cracks did not develop in this alloy as in the case of AA2055-T6.

Table 8 Parameters obtained by PSD for at heat-treatment condition and exposed in a 3.5 wt. % NaCl, 1 wt

Solutions	Materials	Heat treatment condition	Ψ^0(dBi)	*B* (dB(V))	*B* (dB(A))
NaCl	AA2099	T0	− 127.03	− 14.2	− 8.1
		T6	− 132.9	− 11.7	− 9.9
		T8	− 143.7	− 3.6	− 3.5
	AA2055	T0	− 130.5	− 10.2	− 8.2
		T6	− 146.7	− 12.0	− 8.0
		T8	− 141.4	− 11.7	− 3.5
HCl	AA2099	T0	− 110.9	− 9.3	− 12.7
		T6	− 113.9	− 5.6	− 8.2
		T8	− 112.5	− 7.8	− 9.2
	AA2055	T0	− 112.5	− 9.7	− 12.0
		T6	− 115.1	− 11.3	− 12.6
		T8	− 118.7	− 11.8	− 12.9
H_2SO_4	AA2099	T0	− 121.0	− 9.7	− 9.2
		T6	− 126.7	− 5.7	− 14.4
		T8	− 125.9	− 8.0	− 19.4
	AA2055	T0	− 126.14	− 9.8	− 9.6
		T6	− 146.95	− 10.0	− 9.1
		T8	− 114.9	− 8.4	− 15.0

It is also notable that solutions containing Cl^- ions are more aggressive, in this case NaCl and HCl solutions. The Cl^- ion has the characteristic of strong penetration or adsorption and reduces the protection of the passive layer, subsequently this leads to the evolution of hydrogen during anodic dissolution [70]. It has also been reported that the corrosion potential of the T1 phase in a 3.5% NaCl solution is − 1096 mV (vs SCE) [79], which is 346 mV more negative than that corresponding to Al (− 750 mV (vs SCE)) [80]. As a consequence of the high electronegativity of the T1 phase, localized corrosion is promoted in regions containing relatively high-volume fractions of the T1 phase.

It has been suggested by some investigators that at T6 and T8 conditions, Al alloys might be susceptible to severe localized corrosion in environments containing chloride ions. Buchheit et al. [16, 76, 77] found that pitting corrosion in an AF/C 458 alloy was related to constituent particles that promote attack at the grain/subgrain boundary. He also reported that the T1(Al_2CuLi) phase was the main cause of the attack at the grain/subgrain boundary. On the other hand, Li et al. [13], when studying Al–Li alloys by electrochemical impedance spectrometry, reported that in T6 condition there is a greater susceptibility to exfoliation corrosion compared to the alloy in T8 condition. Similarly, it has been suggested by several authors [81–83] that the distribution of the T1 phase inside the grains depends on their orientation with respect to the direction of cold working, since grains with different orientations have different amounts and types of slip systems and, therefore, they are subject to different degrees of deformation. Thus, a greater number of dislocations could be introduced in the grains that reach greater deformation. As already mentioned, dislocations and grain boundaries are preferential sites for nucleation of precipitates; therefore, there would be a non-uniform distribution of such hardening precipitates, which promotes preferential sites for localized corrosion. Although the susceptibility to corrosion of alloys in T6 and T8 conditions has been reported, corrosion studies of Al alloys in T0 condition are very scarce. In the present investigation, the high susceptibility to corrosion of alloys in T0 condition has been observed and has been related to the high number of particles precipitated during the treatment, which is definitely higher than in T6 and T8 conditions.

Conclusions

1. The alloys in the T0 heat-treatment condition presented the lowest Vickers microhardness, followed by the alloys in the T6 condition, and finally the alloys in the T8 condition presented the highest microhardness values. This increase in microhardness is due to the better distribution and higher density of hardening phases T1 and S within the grain boundaries, promoted by cold deformation.
2. The AA2055-T0 alloy presented a high amount of second-phase particles in its microstructure. The AA2055-T6 alloy developed cracks along the grain boundaries, probably due to temperature gradients present during treatment. The AA2099-T0 alloy presented very few second-phase particles. In T8 condition, the alloys develop hardening precipitates inside the grains and the broadening of the Cu shortage zones is decreased.
3. The alloys that presented a greater susceptibility to corrosion were AA2055-T0, AA2055-T6, and AA2099-T6. This is attributed to the number of precipitated particles with different potentials from the matrix to the formation of cracks in AA2055-T6 and to precipitation at grain boundaries, as well as to the presence of Cu-scarce zones. The alloys with the best corrosion performance were AA2099-T0, AA2099-T8, and AA2055-T8, although the last two alloys also present better microhardness measurements.
4. Superior corrosion kinetics were also observed in the presence of 3.5% NaCl and 1% HCl. This could be due to the presence of the Cl^- ion, which has the characteristic of strong penetration or adsorption and reduces the protection of the passive layer. Subsequently, this leads to the evolution of hydrogen during anodic dissolution.

References

1. Sahul M, Sahul M, Harsáni M, Dománkova M (2020) On the microstructure and mechanical properties of AW2099 aluminum lithium alloy joints produced with electron beam welding. Mater Lett 276:128276
2. Gao C, Gao R, Ma Y (2015) Mater Design 83:719–727
3. Lee HS, Yoon JH, Yoo JT (2016) Friction stir welding process of aluminum-lithium alloy 2195. Procedia Eng 149:62–66
4. Zhang F, Shen J, Yan XD, Sun JL, Sun XL, Yang Y (2014) Homogenization heat treatment of 2099 Al-Li alloy. Rare Met 33:28–36
5. Rioja RJ, Liu J (2012) The evolution of Al-Li base products for aerospace and space applications. Metall Mater Trans 43A:3325–3337
6. Dursun T, Soutis C (2014) Recent developments in advanced aircraft aluminum alloys. Mater Des 56:862–871
7. Li M, Hu L, Huang W, Yang X, Guo Y (2022) Effects of T1/T2 precipitates on deformation behavior and microstructure evolution of AA2099 Al-Li alloy: experimental investigation and crystal plasticity finite element modeling. J Mater Res And Tech 17:342–352
8. Zheng X, Luo P, Yue G, Hu Y (2021) Analysis of microstructure and high-temperature tensile properties of 2060 Al-Li alloy strengthened by laser shock peening. J Alloys Compd 860:158539
9. Wanhill RJ (1994) Status and prospects for aluminium-lithium alloys in aircraft structures. Int J Fatigue 16(3):20. https://doi.org/10.1016/0142-1123(94)90441-3

10. Muhammed J, Adinoyi NM, Jafar A (2018) Shear fatigue behavior of AW2099-T83 aluminum-lithium alloy. Int J Fatigue 117:101–110
11. Li JF, Li CX, Peng ZW, Chen WJ, Zheng ZQ (2008) Corrosion mechanism associated with T1 and T2 precipitates of Al-Cu-Li alloys in NaCl solutions. J Alloy Compd 460:688–693
12. Proton V, Alexis J, Andrieu E, Delfosse J, Deschamps A, De Geuser F, Lafont M, Blanc C (2014) The influence of artificial ageing on the corrosion behavior of a 2050 aluminum-copper-lithium alloy. Corros Sci 80:494–502
13. Li JF, Zheng ZQ, Li SC, Chen WJ, Ren WD, Zhao XS (2007) Simulation study on function mechanism of some precipitates in localized corrosion of Al alloys. Corros Sci 49:2436–2449
14. Ma Y, Wu H, Zhou X, Li K, Liao Y, Liang Z, Liu L (2019) Corrosion behavior of anodized Al-Cu-Li alloy: the role of intermetallic particle introduced film defects. Corros Sci 158:108110
15. Ma Y, Zhou X, Liao Y, Yi Y, Wu H, Wang Z, Huang W (2016) Localized corrosion in AA2099-T83 aluminum-lithium alloy: the role of grains orientation. Corros Sci 107:41–48
16. Buchheit RG, Moran JP, Stoner GE (1994) Electrochemical behavior of the T1(Al_2CuLi) intermetallic compound and its role in localized corrosion of Al-2%Li-3%Cu alloys. Corrosion 50:120–130
17. Buchheit RG, Mathur D, Gouma PI, Shaw BA (2001) In: Buchheit, RG, Moran JP (Eds.) Corrosion and Corrosion Prevention of low-density Metals and Alloys. The Electrochemical Society. Pennington, New Jersey
18. Guéring M, Alexis J, Andrieu E, Laffont L, Lefebvre W, Odemer G, Blanc C (2016) Identification of the metallurgical parameters explaining the corrosion susceptibility in a 2050 aluminum alloy. Corros Sci 102:291–300
19. Ma Y, Zhou X, Huang W, Thomson GE, Zhang X, Luo C, Sun Z (2015) Localized corrosion in AA2099-T83 aluminum-lithium alloy: the role of intermetallic particles. Mater Chem Phys 161:201–210
20. Wu H, Ma Y, Huang W, Zhou X, Li K, Liao Y, Wang Z, Liang Z, Liu L (2018) Effect of iron-containing intermetallic particles on film structure and corrosion resistance of anodized AA2099 alloy. J Electrochem Soc 165:C573–C581
21. Peltier F, Thierry D (2021) Localized corrosion of intermetallic particles on aluminum AA2099-T8. Corros Eng Sci Tech 56(7):610–617
22. Prasad KS, Prasad NE, Gokhale AA (2014) Microstructure and precipitate characteristics of aluminum-lithium alloys. Chapter 4, p 99–137
23. Smialowska ZS (1999) Pitting corrosion of aluminum. Corros Sci 41:1743–1767
24. Gloria A, Montanari R, Richeta M, Varone A (2019) Alloys for aeronautic application: state of the art and perspectives. Metals 9:662
25. Mouritz AP (2012) Introduction to aerospace materials. Elsevier, Woodhead Publishing Ltd, Cambridge, England
26. Balducci E, Ceschini L, Messiere S, Wenner S, Holmestad R (2017) Effects of averaging on microstructure and tensile properties of the 2055 Al-Cu-Li-Ag alloy. Mater Sci Eng A 707:221–231
27. Alcoa, Alloy 2099-T83 and 2099-T8E67 (2005) Extrusions. www.alcoa.com/adip/catalog/pdf/Alloy2099TechSheet.pdf
28. Decreus B, Deschamps A, De Geuser F, Donnadieu P, Sigli C, Weyland M (2013) The influence of Cu/Li ratio on precipitation in Al-Cu-Li-x alloys. Acta Mater 61:2207–2218
29. Zhou Y, Liu Z, Bai S, Ying P, Lin L (2017) Effect of Ag additions on the lengthening rate of Ω plates and formation of σ phase in Al-Cu-Mg alloys during thermal exposure. Mater Charact 123:1–8
30. Bai S, Ying P, Liu Z, Wang J, Li J (2017) Quantitative transmission electron microscopy and atom probe tomography study of Ag -dependent precipitation Ω phase in Al-Cu-Mg alloys. Mater Sci Eng 687A:8–16
31. Singh V, Mukhopadhyay A, Prasad K (1997) Influence of small additions of zinc on the nature of the grain boundary precipitates in AA8090 alloy. Scripta Mater 37:1519–1523
32. Luo C, Albu SP, Zhou X, Sun Z, Zhang X, Tang Z, Thompson GE (2016) Continuous and discontinuous localized corrosion of a 2xxx aluminum-copper-lithium alloy in sodium chloride solution. J Alloys Comp 658:61–70
33. Li S, He Ch, Fu J, Xu G (2020) Evolution of microstructure and properties of novel aluminum-lithium alloy with different roll casting process parameters during twin-roll casting. Mater Charact 161:110145
34. Liu Q, Zhu R, Liu DY, Xu Y, Li J, Chen Y, Zhang X, Zheng Z (2017) Correlation between artificial aging and intergranular corrosion sensitivity of a new Al-Cu-Li alloy sheet. Mater Corros 68:65–76
35. Jiang B, Wang H, Tian Yu, Yi D, Liu H, Hu Z (2020) Effects of aging time on corrosion behavior of an Al-Cu-Li alloy. Corros Sci 173:108759
36. Lei X, Saatchi A, Ghanbari E, Dang R, Li W, Wang N, Macdonald D (2019) Studies on pitting corrosion of Al-Cu-Li alloys part I: effect of Li addition by microstructural, electrochemical, in-situ, and pit depth analysis. Materials 12:1600
37. Jiang B, Yi D, Yi X, Zheng F, Wang H (2018) Effect of trace of added Sc on microstructure and mechanical properties of 2055 aluminum alloy. Mater Charact 141:248–259
38. Sainfort P, Dubost B (1987) Coprecipitation hardening in Al-Li-Cu-Mg alloys. J Phys C3(9):407–413
39. The Aluminum Association International. International Alloy. Designation and Chemical Compositions Limits for Wrought Aluminum and Wrought Aluminum alloys With Support for On-Line Access From: Aluminum Extruders Council Use for the Information; The Aluminum Association (2015) Arlington County. Va, USA
40. Chandler H (1996) Heat treater's guide. practices and procedures for nonferrous alloys. The materials information company
41. Romios M, Tirashi R, Ogren JR (2005) Design of multistep aging treatments of 2099(C458) Al-Li alloy. J of Mater Eng and Perform 14:641–646
42. Int ASTM (2017) Standard guide for preparation of metallographic specimen E3–11:1–17
43. Int ASTM (2004) Metallography and microstructure. ASM Handbook 9:2004
44. ASTM Int Standard guide test methods for micro indentation hardness of materials. E384
45. ASTM Int (2009) Standard guide for electrochemical noise measurement. G199 ASTM. EUA
46. Yoshimura R, Konno TJ, Abe E, Hiraga K (2003) Transmission electron microscopy study of the evolution of precipitates in aged Al-Li-Cu alloy: the q' y T1 phases. Acta Mater 51:4251–4266
47. Bugarin AF, De Abreu C, Terada M, De Melo HG, Costa I (2020) Effect of friction stir welding (FSW) on the electrochemical behaviour and galvanic coupling of AA2024-T3 and AA7475-T651. Mater Today Commun 25:101591
48. King F (1992) El aluminio y sus aleaciones. México. LIMUSA
49. Lumley R, Metson J, Kvande H, Wallace G, Grandfield JF, Otarawanna S (2011) Fundamentals of aluminum metallurgy. Woodhead Publishing Limited
50. Li H, Ling J, Xu Y, Sun Z, Liu H, Zheng X, Tao J (2015) Effect of aging treatment on precipitation behavior and mechanical properties of a novel aluminum-lithium alloy. Acta Metall Sin Engl Lett 28:671–677
51. Sainfort P, Dubost B (1987) Coprecipitation hardening in Al-Li-Cu-Mg alloys. J Phys Colloq 48:407–413
52. Itoh G, Cui Q, Kanno M (1996) Effects of a small additions of magnesium and silver on the precipitation of T1 phase in an Al-4%Cu-1.1%Li-0.2%Zr alloy. Mater Sci Eng 211A:128–137

53. Zhu R, Liu Q, Li J, Xiang S, Chen Y, Zhang X (2015) Dynamic restoration mechanism and physical based constitutive model of 2050 Al-Li alloy during hot compression. J Alloy Compd 650:75–85
54. Samaniego-Gámez PO, Almeraya-Calderón FA, Maldonado-Bandala E, Cabral-Miramontes JA, Nieves-Mendoza D, Olguín-Coca J, López-León LD, Silva-Vidaurri LG, Zambrano-Robledo P, Gaona-Tiburcio C (2021) Corrosion behavior of AA2055 aluminum-lithium alloys anodized in the presence of sulfuric acid solution. Coatings 11:1278
55. Ju H, Liu S, Zhang W, Yang Y, Duan J (2021) Investigation of pitting corrosion and hydrogen evolution of aluminum and AA2024 alloy by simultaneous electrochemical measurements and imaging. Electrochemical Communications 132:107135
56. Ma Y, Zhou X, Meng X, Huang W, Liao Y, Chen X, Yi Y, Zhang X, Thompson G (2016) Influence of thermomechanical treatments on localized corrosion susceptibility and propagation mechanism of AA2099 Al-Li alloy. Trans Nonferrous Met Soc China 26:1472–1481
57. Gaona-Tiburcio C, Aguilar LMR, Zambrano-Robledo P, Estupiñan-López F, Cabral-Miramontes JA, Nieves-Mendoza D, Castillo-González E, Alemaraya-Calderón F (2014) Electrochemical noise analysis of níckel based superalloys in acid solutions. Int J Electrochem Sci 9:523–533
58. Montoya-Rangel M, de Garza-Montes ON, Gaona-Tiburcio C, Colás R, Cabral-Miramontes JA, Nieves-Mendoza D, Maldonado-Bandala E, Chacón-Nava J, Almeraya-Calderón F (2020) Electrochemical noise measurements of advanced high-strength steels in different solutions. Metals 10:1232
59. Sanchez JM, Cottis RA, Botana FJ (2005) Shot noise and statistical parameters for the estimation of corrosion mechanisms. Corros Sci 47:3280–3299
60. Mansfeld F, Sun Z, Hsu CH, Nagiub A (2001) Concerning trend removal in electrochemical noise measurements. Corros Sci 43:341–352. https://doi.org/10.1016/S0010-938X(00)00064-0
61. Gusmano G, Montespereli G, Pacetti S, Petitti A, Dámico A (1997) Electrochemical noise resistance as a tool for corrosion rate prediction. Corrosion 53:860. https://doi.org/10.5006/1.3290271
62. Cottis R, Turgoose S, Mendoza J (1996) The effects of solutions resistance on electrochemical noise resistance measurements: a theorical analysis. Electrochemical noise measurements for corrosion applications. ASTM STP 1277. Philadelphia. PA: 93–100
63. Cottis RA, Turgoose S, Neuman R (1999) Corrosion testing made easy: impedance and noise analysis. NACE international: Houston, TX, USA
64. Stern M, Geary AL (1957) Electrochemical polarization. I. A theoretical analysis of the shape of the polarization curves. J Electrochem Soc 104:56–63. https://doi.org/10.1149/1.2428496
65. Jáquez-Muñoz JM, Gaona-Tiburcio C, Cabral-Miramontes J, Nieves-Mendoza D, Maldonado-Bandala E, Olguín-Coca J, López-León LD, Flores-De los Rios JP, Almeraya-Calderón F (2021) Electrochemical noise analysis of the corrosion of titanium alloys in NaCl and H_2SO_4 solutions. Metals 11:105. https://doi.org/10.3390/met1010105
66. Mansfeld F, Sun Z (1999) Localization index obtained from electrochemical noise analysis. Corrosion 55:915–918
67. Reid SA, Eden DA (2001) Assessment of corrosion. a method and apparatus for using EN to assess corrosion. preferably with skewness and kurtosis analysis using neural nets. U.S. 6: 264,824 B1
68. Cottis R (2001) Interpretation of electrochemical noise data. Corrosion 57:265–285
69. Pedemonte JM, Bárcena MM (2002) Ruido electroquímico. Métodos de análisis. Septem Ediciones. ISBN: 84-95687-33-X
70. Obot IB, Ikenna B, Zeino A (2019) Electrochemical noise (EN) technique: review of recent practical applications to corrosion electrochemical research. J Adhes Sci Technol 33(13):1453–1496
71. Bertocci U, Huet F (1995) Noise analysis applied to electrochemical systems. Corrosion 51:131–144
72. Lee CC, Mansfeld F (1998) Analysis of electrochemical noise data for a passive system in the frequency domain. Corr Sci 40:959–962
73. Cabral-Miramontes JA, Barceinas-Sánchez JDO, Poblano-Salas CA, Pedraza-Basulto GK, Nieves-Mendoza D, Zambrano-Robledo PC, Almeraya-Calderón F, Chacón-Nava JG (2013) Corrosion behavior of AISI 409Nb stainless steel manufactured by powder metallurgy exposed in H_2SO_4 and NaCl solutions. Int J Electrochem Sci 8:564–577
74. Botana J, Marcos M, Aballe A (2002) Ruido Electroquímico. Métodos de Análisis. Editor: Speten Ediciones. pp. 1–128
75. Mansfeld F, Sun Z, Hsu CH (2001) Electrochemical noise analysis (ENA) for active and passive systems in a chloride media. Electrochim Acta 46:3651–3664. https://doi.org/10.5006/1.3283926
76. Buchheit RG, Moran JP, Stoner E (1994) Localized corrosion behavior of alloy 2090. The role of microstructural heterogeneity Corrosion 46:610–617
77. Kertz JE, Gouma PI, Buchheit RG (2001) Localized corrosion susceptibility of Al-Li-Cu-Mg-Zn alloy AF/C 458 due to interrupted quenching from solutionizing temperatures. Metal. And Mat. Trans. A: Phys. Metal and Mat Sci 32:2561–2573
78. Kumai C, Kusinski J, Thomas G, Devine T (1989) Influence of aging at 200 °C on the corrosion of Al-Li and Al-Li-Cu alloys. Corrosion 45:294–302
79. Buchheit RG (1995) A compilation of corrosion potentials reported for intermetallic phases in aluminum alloys. J Electrochem Soc 142(11):3994–3996
80. Vargel C, Jacques M, Schmidt MP (2004) Corrosion of aluminum. Elsevier, Oxford
81. Hansen N, Jensen DJ (1999) Development of microstructure in FCC metals during cold work. Philosop Trans Roy Soc London 357(1756):1447–1469
82. Liu Q, Jensen DJ, Hansen N (1998) Effect of grain orientation on deformation structure in polycrystalline aluminum. Acta Mater 46(16):5819–5838
83. Godfrey A, Hansen N, Jensen DJ (2007) Microstructural based measurement of local stored energy variations in deformed metals. Metall Mater Trans A Phys Metall Mater Sci 38(13):2329–2339